Towards the production of carbon xerogel monoliths by optimizing convective drying conditions

Nathalie Job, Françoise Sabatier, Jean-Paul Pirard, Michel Crine, Angélique Léonard*

University of Liège, Department of Applied Chemistry, Laboratory of Chemical Engineering, B6c - Sart-Tilman, 4000 Liège, Belgium

Abstract

Resorcinol-formaldehyde hydrogels prepared at various resorcinol/sodium carbonate ratios, *R/C*, were convectively air dried. The influence of the drying operating conditions, *i.e.* air temperature and velocity, on the pore texture, shrinkage and cracking of the dried gels were investigated. Shrinkage was found to be isotropic. The shrinkage behaviour and the textural properties of the gels are independent of the drying operating conditions, but are completely determined by the value of the synthesis variables. The analysis of the drying kinetics shows two main drying periods. During the first phase, shrinkage occurs and the external surface of the material remains completely wet: heat and mass transfers are limited by external resistances located in a boundary layer. When shrinkage stops, the second period begins: the evaporation front recedes inside the solid and internal transfer limitations prevail. The drying time can be reduced by increasing the air temperature and/or velocity, but the temperature increase is limited when monolithicity is required, especially when the pores are small. For example, at a temperature of 160°C and a velocity of 2 m/s, about 1 h is needed to dry a 2.8 cm in diameter and 1 cm in height cylinder containing macropores (pore width > 50 nm after drying). The same cylinder presenting small mesopores (pore width = 10 to 15 nm after

*Corresponding author. Tel.: +32 4 366 47 22; Fax: +32 4 366 28 18; E-mail address: A.Leonard@ulg.ac.be

drying) requires 20 h at 30°C and 2 m/s to reach complete dryness without the development of cracks.

Keywords: Carbon xerogels; Porous carbon; Heat treatment; Texture.

1. Introduction

Organic gels are usually dried under supercritical conditions in order to avoid surface tensions and shrinkage due to the appearance of liquid-vapour curved interfaces [1-2]. Even though some attempts have been made to simplify the drying procedure by using freeze-drying [3] or solvent exchange followed by evaporation [4], drying processes used up to now remain time consuming, expensive and discontinuous, which hampers the transition to an industrial scale production.

Previous works showed that vacuum drying [5-6] and convective drying [7-8], without any pre-treatment, can be used to obtain porous organic gels, provided that adequate synthesis conditions are adopted. After pyrolysis, highly porous carbon materials presenting a wide range of pore textures are obtained. Nevertheless, vacuum drying remains difficult to apply industrially. On the contrary, convective drying can be conducted continuously under atmospheric conditions, which can lead to larger productivities and lower production costs.

This work focuses on the production of cracks free resorcinol(R)-formaldehyde(F) xerogels, which is an essential step before pyrolysis and production of monolithic carbon materials. Though not always required, monolithicity is crucial in some applications like electrodes or supercapacitors. When the mechanical strength of the network is high enough to withstand the capillary pressures resulting from evaporation in the pores, the collapse of the pore texture can be avoided. However, when the drying conditions are too severe, cracking may occur. In this study, the influence of the drying conditions, *i.e.* air temperature and velocity, on the shrinkage, the cracking and the textural properties of the xerogels were investigated. Since drying kinetics are strongly related to the material textural properties, especially to the pore size, three different synthesis conditions were tested in this work. Indeed, the pore texture of the pristine RF hydrogels can be modified by changing the pH, or the *R/C* ratio, of the precursors solution. The effect of the *R/C* value on the pore size was already discussed in many previous studies reviewed by Muhtaseb and Ritter [2]. As a rule, the pore size and pore volume increase when *R/C* increases.

Results show no influence of the drying conditions on the pore texture: the extent of shrinkage and the final pore volume are completely determined by the synthesis conditions. However, the drying rate must be carefully controlled when monolithicity is required: cracks, leading to the sample breakage, appear when drying is too severe, especially with samples displaying small pores, *i.e.* which are synthesized at high pH.

2. Experimental

2.1. Preparation of RF hydrogels

Hydrogels with various pore textures were prepared by polycondensation of resorcinol, solubilized in water, with formaldehyde, in the presence of Na_2CO_3. Three different pH of the precursors solution were achieved by changing the Resorcinol/Sodium carbonate molar ratio, *R/C*, fixed at 300, 500 and 1000. The resorcinol-formaldehyde molar ratio, *R*/*F*, and the dilution ratio, *D*, *i.e.* the *Solvent*/(*R*+*F*) molar ratio, were fixed at 0.5

(stoichiometric ratio), and 5.7, respectively. The total amount of solvent takes into account the deionised water added but also water and methanol (stabilizer) included in the formaldehyde solution. 9.91 g resorcinol (VWR International, 99%) were first mixed with 18.8 ml deionised water with the required amount of Na_2CO_3 in 250 ml sealable flasks under magnetic stirring. The formaldehyde solution (Aldrich, 37% wt. in water, stabilized by 10–15% wt. methanol) was poured into a separated flask. All the solutions were then placed in a thermostated bath at 70°C. After temperature stabilisation, 13.5 ml formaldehyde were added to the resorcinol solution. Cylindrical samples were obtained by casting 6 ml solution into glass moulds (diameter = 28 mm) and putting them back in the water bath for gelation and aging during 24 h at 70°C. A second cylindrical mould, slightly smaller in diameter, was slipped into the first one and put in touch with the solution so that the contact between air and liquid was avoided. Evaporation was prevented by a paraffin film covering both cylinders. This procedure aims at avoiding thermal inertia and temperature gradients during the gelation phase. Moreover, the size of the samples was adapted to both the convective dryer chamber and the microtomograph used to follow shrinkage and cracking during drying.

2.2. Convective drying of monoliths

After gelation and aging, the monoliths were dried in a classical convective rig controlled in air relative humidity, temperature and velocity specially designed for the handling of small samples (a few cm^3) [9]. The sample was continuously weighed during the drying test. Its mass was recorded every 10 s. The sample surroundings were designed so that drying could occur on the whole external surface. Drying curves, representing the drying rate (kg_{water}/s) *vs.* the water content on a dry basis, W ($kg_{water}/kg_{dry\ solid}$), were calculated from the mass evolution. Dividing the drying rate by the external exchange area measured by X-ray tomography [10] yields to the so-called Krischer's curves, *i.e.* the mass flux F ($\text{kg}_{\text{water}}/(\text{m}^2.\text{s})$) *vs.* water content, W, commonly used to study drying [11].

Preliminary tests were carried out at 115°C and 2 m/s in order to determine whether the gels remained monolithic or not under these drying conditions. From the results, an experimental program was designed for each R/C value. For $R/C = 1000$, no breakage was observed. Three temperatures were thus tested (70, 115 and 160°C) at a superficial velocity of 2 m/s. Three air velocities (1, 2 and 3 m/s) were tested at the intermediate temperature (115°C). For $R/C = 300$, the preliminary test led to the cracking of the gel. Consequently, the temperature was progressively reduced (70, 50 and 30°C) to find operating conditions avoiding cracking. The influence of air velocity was studied at T = 50°C. For $R/C = 500$, intermediate drying temperatures of 70, 92.5 and 115°C were adopted and sensitivity towards velocity was studied at 92.5°C.

2.3. X-ray microtomography

X-ray tomography is a non-invasive technique allowing the visualization of the internal texture of a material. An original methodology using X-ray microtomography coupled to image analysis was previously developed [12] to follow the textural evolutions of samples, *i.e.* shrinkage and cracks development, during a drying operation. Traditionally, the measurement of shrinkage occurring during drying is performed by destructive or poorly accurate techniques such as volume displacement methods. Cracks detection and quantification are realised either by destructive techniques or sophisticated but expensive non destructive ones (NMR imaging). X-ray microtomography, in combination with image analysis, provides an accurate, non destructive and easy to use technique to determine simultaneously shrinkage and crack extent.

During tomographic investigation, an X-ray beam is sent on the sample and the transmitted beam is recorded with a detector. According to Beer-Lambert law, the transmitted intensity is related to the integral of the X-ray attenuation coefficient along the path of the beam, μ. This coefficient μ depends on the material density, ρ, the atomic number of the material, Z, and on the energy of the incident beam, E, according to Eq (1):

$$\mu = \rho\left(\mathrm{a} + \frac{\mathrm{b}Z^{3.8}}{E^{3.2}}\right) \tag{1}$$

where a is a quantity with a relatively small energy dependence, and b is a constant [13]. Projections (defined by the assembling of transmitted beams) are recorded for several angular positions by rotating the sample between 0 and 180°. Then a back-projection algorithm is used to reconstruct 2D or 3D images, depending on the method used. In the case of 2D images, each pixel is characterized by a grey level value corresponding to the local attenuation coefficient.

The X-ray microtomographic device used in this study was a "Skyscan-1074 X-ray scanner" (Skyscan, Belgium). Advanced technical details about its conception and operation are described by Sasov and Van Dyck [14]. The X-ray source operates at 40 kV and 1 mA. The detector is a 2D, 768×576 pixels, 8-bit X-ray camera with a spatial resolution of 41 µm.

A drying test was monitored by continuously weighing the sample until drying completion, *i.e.*, until a stable weight *vs.* time was observed. In order to follow the sample shrinkage and to detect the appearance of cracks, it is necessary to interrupt the drying procedure at different time intervals, to remove the sample from the drying chamber and to insert it for a while into the X-ray microtomographic cell. The sample was replaced in the micro-dryer after approximately 2 min. The rotation step was fixed at 3.6° in order to reduce the acquisition time down to 2 min; this angle interval allows to obtain 50 radiographs of the sample. Limiting the acquisition time is necessary to avoid the relaxation of moisture profiles and further drying of the sample. Cross sections separated by 0.41 mm were reconstructed using a cone-beam reconstruction software. Image analysis procedures developed previously [12,15] enabled us to determine the height of the sample from the radiographs, and the equivalent diameter from the cross-sections. The evolution xerogel volume, *i.e.* the shrinkage, as a function of the water content were obtained from the knowledge of both the diameter and height. The evolution of the external surface area of the sample was used to obtain the Krischer's curve, *i.e.* the drying flux, F, *vs.* the water content, W.

2.4. Texture characterization

The pore texture of the RF xerogels was characterized by analysis of the nitrogen adsorption-desorption isotherms, determined at 77 K with a Sorptomatic Carlo Erba 1900 and by mercury porosimetry with a Thermofinnigan Pascal 140 porosimeter. The samples were outgassed at 10^{-3} Pa during 16 h prior to nitrogen adsorption. Mercury porosimetry measurements were performed between 0.01 and 200 MPa after outgassing during 2 h at 10^{-3} Pa. The bulk density of the samples, ρ_{bulk}, was derived from mercury pycnometry.

The analysis of the nitrogen adsorption-desorption isotherms was performed according to the methodology proposed by Lecloux [16] in order to determine the BET specific surface area, S_{BET}, the micropore volume calculated by the Dubinin–Radushkevich equation, V_{DUB}, and the pore volume calculated from the adsorbed volume at saturation, V_{p}. In the case of samples containing micropores and mesopores only (pore size < 50 nm) and whose isotherm displays a plateau at saturation, adsorption data are precise enough to determine the total pore volume of the sample, V_v: indeed, $V_v = V_p$. However, pore volume measurements by nitrogen adsorption are not precise enough for samples containing macropores, *i.e.* pores of width larger than 50 nm, corresponding to relative pressures $p/p_0 > 0.98$ following the Kelvin equation. In the case of macroporous samples, the specific volume measured by mercury porosimetry was combined with the adsorption data to calculate the total pore volume, V_v. Since mercury porosimetry is limited to pores larger than about 7.5 nm, the total pore volume, V_v, is calculated by Eq. 2 [17]:

$$V_v = V_{DUB} + V_{cum<7.5nm} + V_{Hg} \qquad (2)$$

where V_{DUB} is the micropore volume (pores of width lower than 2 nm), V_{Hg} is the specific pore volume measured by mercury porosimetry, and V_{cum} < 7.5 nm is the cumulative volume of pores of width between 2 and 7.5 nm determined by the Broekhoff–de Boer theory [16].

Since crushing occurs in most samples during mercury porosimetry measurements, Washburn’s law [18] cannot be used for the determination of the pore size distribution. The theory introduced by Pirard et al. [19-20], which directly relates the pore size to the mercury pressure, can be used when collapse occurs only, *i.e.* when the pores of decreasing size are successively completely eliminated by crushing as the mercury pressure increases. This mechanism implies then a total compaction of the pores of size larger than a given limit, the pores of smaller size remaining unchanged. However, it seems that RF xerogels do not collapse but that all the pores are compressed simultaneously [21]. Therefore, their size would decrease during compression and no relationship between the mercury pressure and the pore size could be deduced. Though no pore size distribution can be pertinently established at the moment, the porosimetry curves can be compared in order to highlight similarities or differences between xerogels. Moreover, whatever the mechanism (intrusion or crushing), it is to be noted that the recorded volume V_{Hg} corresponds to the cumulative volume of pores larger than 7.5 nm [22]. As a consequence, Eq. (2) remains valid whatever the mechanism.

2.5. Sample designation

The samples are denoted as follows: the letter X (for xerogel) is followed by the values of the *R/C* ratio, the drying temperature (°C) and air velocity (m/s). For example, the sample X-1000-115-2 corresponds to a gel synthesized with *R*/*C* = 1000 and convectively dried at a temperature of 115°C, the air velocity being fixed at 2 m/s.

3. Results

3.1. Shrinkage behaviour

Figs. 1 and 2 display the shrinkage curves, *i.e.* the sample volume divided by its initial value *vs.* the normalized water content, obtained for the three *R/C* ratios under various drying conditions. Some curves are incomplete because of the breakage of the sample during drying. Fig. 1 shows that the degree of final shrinkage increases with decreasing *R/C* and is independent of the drying temperature. The volume reduction is about 10-15% when *R/C* = 1000, while the final sample shrinkage reaches about 45% and 60% when *R/C* = 500 and 300, respectively. At *R/C* = 300, the final volume mentioned above is that obtained with sample X-300-30-2; indeed, drying at higher temperature leads to the breakage of the sample. The data obtained at *R/C* = 500 and *R/C* = 300 are characterized by a linear part followed by a plateau that begins when shrinkage stops. The linear part corresponds to ideal shrinkage, *i.e.* a volume reduction corresponding exactly to the volume of removed water. Fig. 2 shows that shrinkage is independent of the air velocity. Moreover, the evolution of height and diameter *vs.* the water content (not shown) are very similar, which indicates that the shrinkage is isotropic.

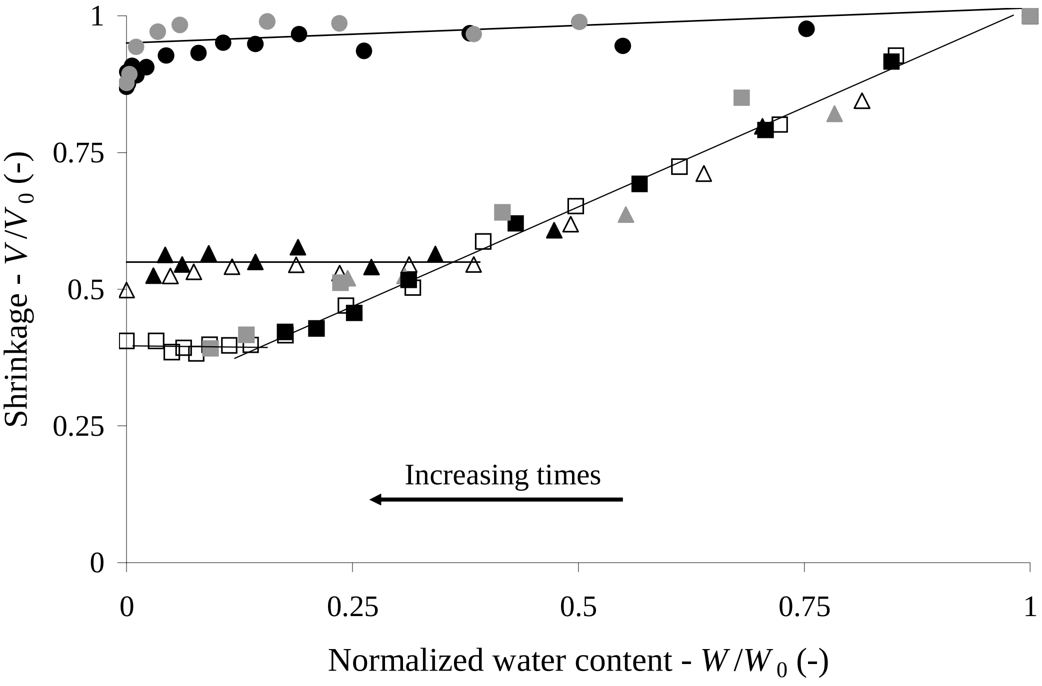

Fig. 1. Shrinkage curves: influence of the drying temperature and *R/C* ratio. v_{air} = 2 m/s. (●) X-1000-70-2; (●) X-1000-115-2; (▲) X-500-70-2; (△) X-500-92.5-2; (▲) X-500-115-2 (incomplete – breakage); (☐) X-300-30-2; (■) X-300-70-2 (incomplete – breakage); (■) X-300-115-2 (incomplete – breakage).

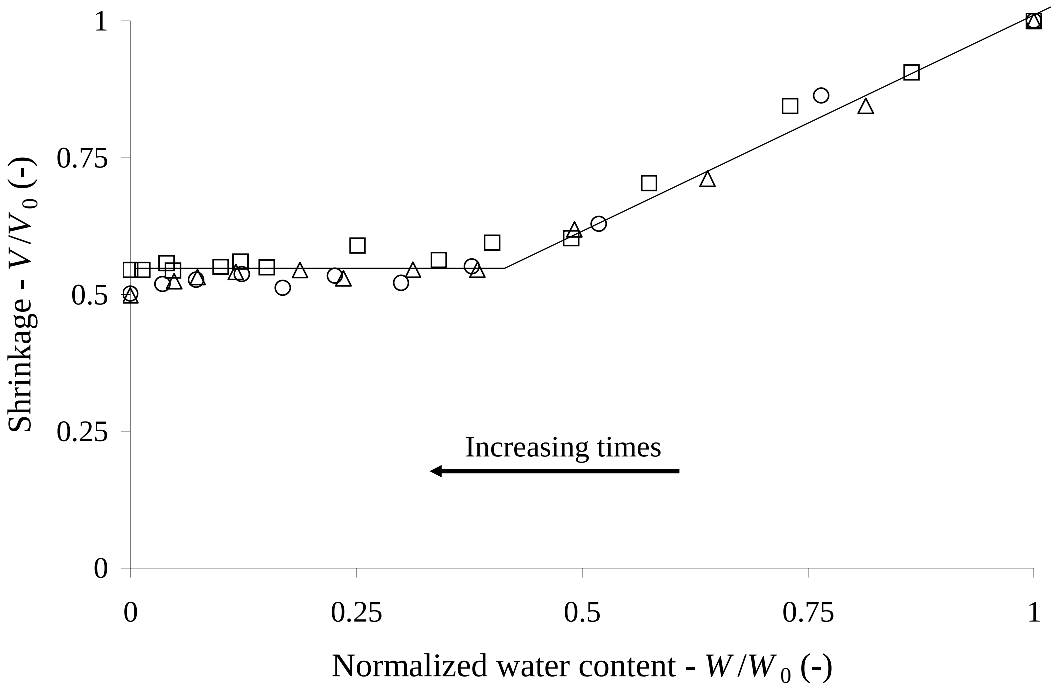

Fig. 2. Shrinkage curves: influence of air velocity. *R/C* = 500 – *T* = 92.5°C. (□) X-500-92.5-1; (△) X-500-92.5-2; (○) X-500-92.5-3.

3.2. Drying kinetics

Table 1 presents some drying characteristics of the fifteen samples: the total weight loss ΔM, the initial water content, W_0, the final volume divided by the initial value, $(V/V_0)_f$, the drying time, t_f, corresponding to mass stabilization, and the final sample state. ΔM and W_0 are almost constant (ΔM = 65.0 to 69.3%; W_0 = 1.86 to 2.25) because these parameters essentially depend on the dilution ratio, *D*, considering that the polycondensation reaction reached the same advancement state for all samples. The drying time depends on both *R/C* and drying conditions. Globally, drying gets faster when (i) *R/C* increases, (ii) the air temperature increases (iii) and the air velocity increases. At constant *R/C* ratio value, the drying time is mostly influenced by temperature. Moreover, the effect of temperature is more pronounced at low *R/C* values. When *R/C* is low, it is very difficult to combine fast drying with the preservation of a monolithic structure. Temperature has to be reduced to 30°C (at v_{air} = 2 m/s) to avoid the cracking and breakage of the sample.

Table 1.

Drying characteristics

Sample	ΔM (%)	W_0 ($\mathrm{kg_{water}/kg_{dry\ solid}}$)	$(V/V_0)_\mathrm{f}$ (-)	t_f (min)	Final state
X-1000-70-2	66.7	2.00	0.87	250	monolith
X-1000-115-1	68.3	2.15	0.85	149	monolith
X-1000-115-2	66.9	2.03	0.88	133	monolith
X-1000-115-3	65.5	1.90	0.85	108	monolith
X-1000-160-2	67.3	2.06	0.87	68	monolith
X-500-70-2	67.8	2.11	0.53	334	monolith
X-500-92.5-1	68.0	2.11	0.55	376	monolith
X-500-92.5-2	68.2	2.14	0.50	250	monolith
X-500-92.5-3	69.3	2.25	0.50	205	monolith
X-500-115-2	68.5	2.18	-[a]	108	fragments
X-300-30-2	65.2	1.89	0.40	1204	monolith
X-300-30-3	65.2	1.87	-[a]	1134	fragments
X-300-50-2	68.6	2.18	-[a]	1069	fragments
X-300-70-2	68.7	2.20	-[a]	416	fragments
X-300-115-2	65.0	1.86	-[a]	167	fragments

ΔM: total weight loss; W_0: initial water content; $(V/V_0)_\mathrm{f}$: final volume divided by the initial volume of the sample; t_f: total drying time.

- [a] not measurable (sample breakage).

Krischer’s curves obtained for RF xerogels synthesized with *R/C* = 500 are plotted in Figs. 3 and 4. The same trends are observed with *R/C* = 300 and *R/C* = 1000. After a short preheating zone, a constant drying flux period is observed, followed by a long decreasing drying flux period. The results clearly show an increase of the drying flux when temperature or air velocity increases. This result is in agreement with the reduction of the drying time observed (Table 1). At the end of drying, the curves corresponding to various air velocities overlap (Fig. 4) while they remain separated when the influence of the temperature is investigated (Fig. 3).

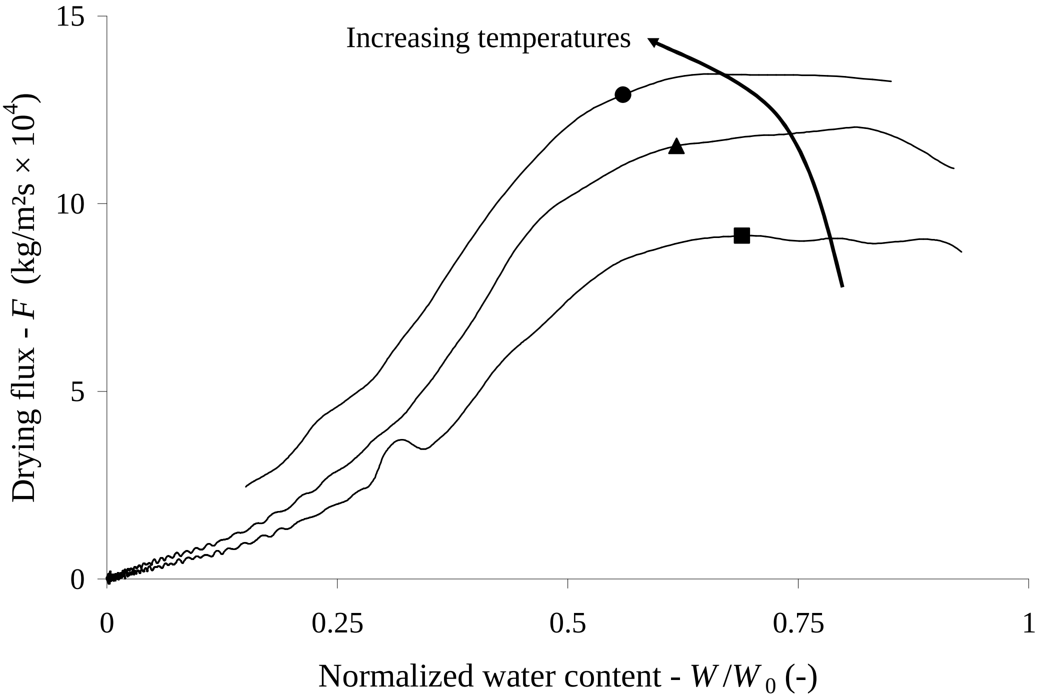

Fig. 3. Krischer’s curves: influence of the drying temperature at *R/C* = 500. (■) X-500-70-2; (▲) X-500-92.5-2; (●) X-500-115-2 (incomplete – breakage).

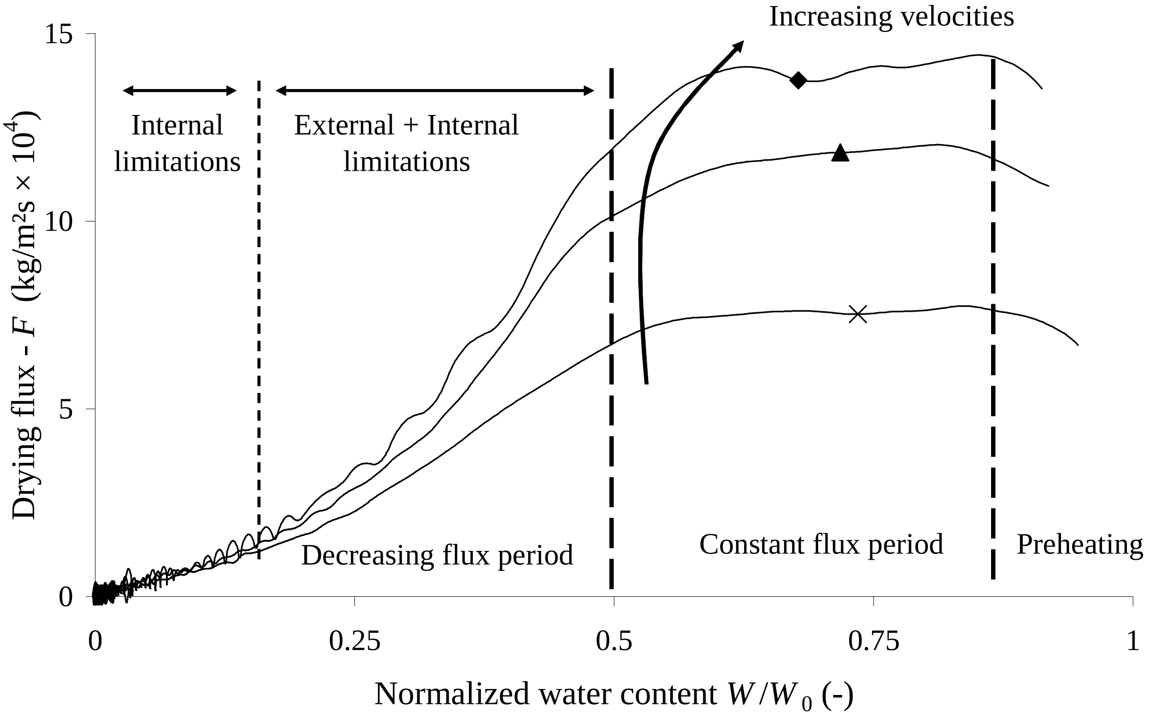

Fig. 4. Krischer’s curves: influence of the air velocity for *R/C* = 500. (▲) X-500-92.5-2; (×) X-500-92.5-1; (◆) X-500-92.5-3.

Fig. 5 shows the influence of *R/C* on the drying flux for a particular set of operating conditions (v_{air} = 2 m/s, T = 70°C). The flux at the plateau, F_c, is almost the same when *R/C* = 300 and *R/C* = 500 but is clearly lower at *R/C* = 1000. At the end of the drying process ($W/W_0 < 0.2$), the three curves overlap.

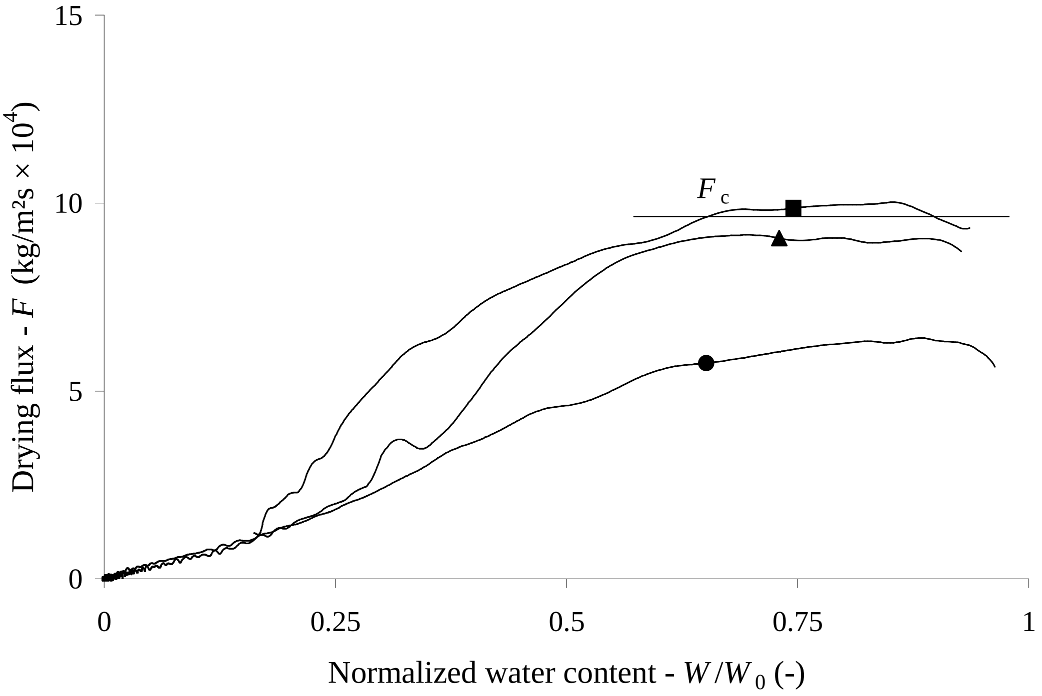

Fig. 5. Krischer's curves: influence of the *R/C* ratio on the drying flux. T = 70°C, v_{air} = 2 m/s. (●) X-1000-70-2; (▲) X-500-70-2; (■) X-300-70-2.

3.3. Evolution of the textural properties during drying: cracking

As indicated in Table 1, some samples remain monolithic while others break during drying. However, some cracks may appear during drying even though the material remains monolithic at the end of the process. Two different behaviours are observed. On the one hand, for the samples obtained with *R/C* = 1000, some cracks appear at the outer border of the cylinder during drying, and then close up progressively at the end of the process because of stress inversion. This is illustrated by cross-section images obtained at decreasing water contents for sample X-1000-115-2 (Fig. 6). Only small traces of cracks can be distinguished on the dried gels. This behaviour was observed for all gels synthesized at *R/C* = 1000. On the other hand, depending on the drying conditions, gels obtained with *R/C* = 500 or *R/C* = 300 remained monolithic (Fig. 7) or cracked. Cracking leads to irreversible breakage in some cases (Fig. 8). The air velocity hardly affects the cracking of the sample, whatever the *R/C* ratio, while the temperature has a great influence. At high *R/C* values, the material withstands high temperatures without development of cracks. On the contrary, relatively low temperature (30°C) has to be used at *R/C* = 300; otherwise the sample completely breaks out.

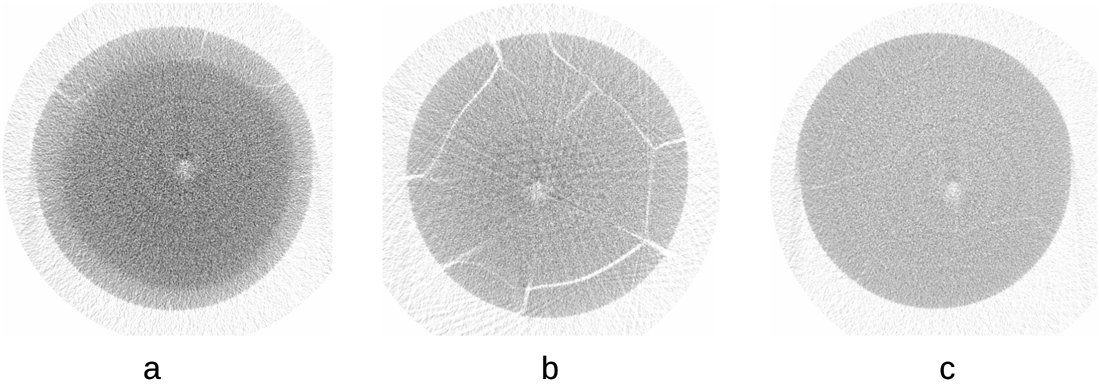

Fig. 6. Sample X-1000-115-2. Cross-sections at various stages of drying. (a) $W/W_0 = 0.23$, (b) $W/W_0 = 0.10$, (c) $W/W_0 = 0.001$.

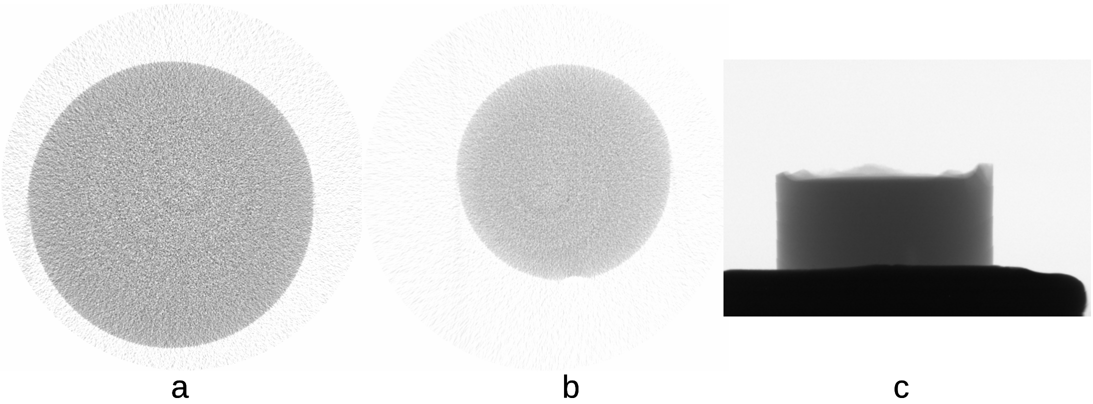

Fig. 7. Sample X-300-30-2. Cross-sections before and after drying (a) $W/W_0 = 1$, (b) $W/W_0 = 0$ and (c) radiograph of the monolith at the end of drying at $W/W_0 = 0$.

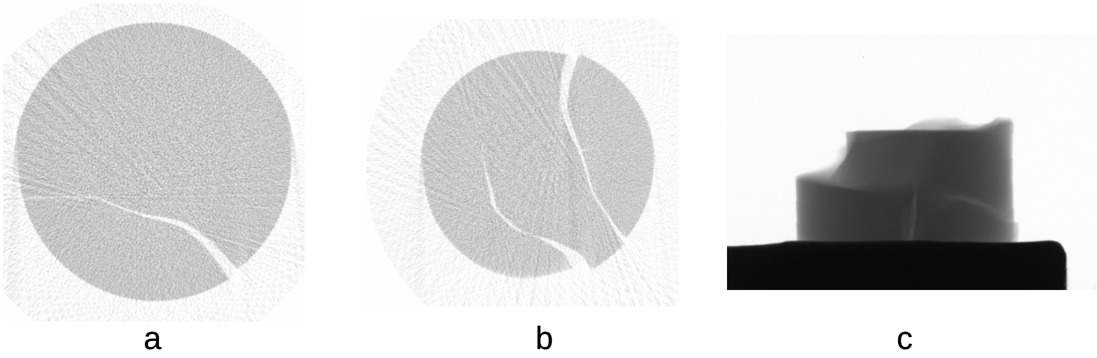

Fig. 8. Sample X-300-70-2. Cross-sections before and after drying (a) $W/W_0 = 1$, (b) $W/W_0 = 0$ and (c) radiograph of the sample at the end of drying at $W/W_0 = 0$.

3.4. Textural properties of the dried gels

Table 2 displays the textural properties of the dried samples. For each R/C ratio, the textural properties, especially the total pore volume, V_v, and the micropore volume, V_{DUB}, are totally independent of the drying conditions.

Typical adsorption-desorption isotherms obtained for each R/C value are displayed in Fig. 9. For a given R/C value, the isotherms are identical whatever the drying conditions. Gels obtained at $R/C = 300$ and $R/C = 500$ are micro-mesoporous (combination of type I isotherm at low p/p_0 and type IV isotherm at high p/p_0), while samples prepared with $R/C = 1000$ are micro-macroporous (combination of type I isotherm at low p/p_0 and type II isotherm at high p/p_0). The pore width is about 10-15 nm and 35-40 nm for samples synthesised at $R/C = 300$ and $R/C = 500$, respectively. Mercury porosimetry measurements were performed on samples containing macropores only ($R/C = 1000$). Fig. 10 shows typical mercury porosimetry curves obtained with these samples. All the curves are practically superimposed. Crushing first occurs up to $P = 30$ MPa, then intrusion begins and goes on up to the maximum mercury pressure. The specific pore volume, V_{Hg}, ranges from 1.72 to 1.86 cm³/g, which is not significantly different.

Table 2.

Textural properties

Sample	S_{BET} (m²/g) ± 5	V_{DUB} (cm³/g) ± 0.01	V_p (cm³/g) ± 0.05	V_{Hg} (cm³/g) ± 0.05	V_v (cm³/g) ± 0.1	ρ_{bulk} (g/cm³) ± 0.02
X-1000-70-2	180	0.09	0.85	1.81	2.0	0.37
X-1000-115-1	165	0.08	0.65	1.86	2.0	0.37
X-1000-115-2	145	0.07	0.65	1.72	2.0	0.36
X-1000-115-3	215	0.09	0.90	1.77	1.9	0.39
X-1000-160-2	130	0.07	0.60	1.82	1.9	0.38
X-500-70-2	315	0.15	0.85	-[a]	0.8	0.67
X-500-92.5-1	325	0.15	0.80	-[a]	0.8	0.68
X-500-92.5-2	315	0.14	0.80	-[a]	0.8	0.69
X-500-92.5-3	315	0.15	0.85	-[a]	0.8	0.68
X-500-115-2	330	0.15	0.80	-[a]	0.8	0.68
X-300-30-2	300	0.13	0.40	-[a]	0.4	0.93
X-300-30-3	300	0.14	0.40	-[a]	0.4	0.94
X-300-50-1	365	0.17	0.35	-[a]	0.4	0.92
X-300-50-2	305	0.14	0.35	-[a]	0.4	0.94
X-300-70-2	295	0.13	0.30	-[a]	0.3	0.98
X-300-115-2	330	0.15	0.35	-[a]	0.4	0.95

-[a] not measured (micro-mesoporous sample).

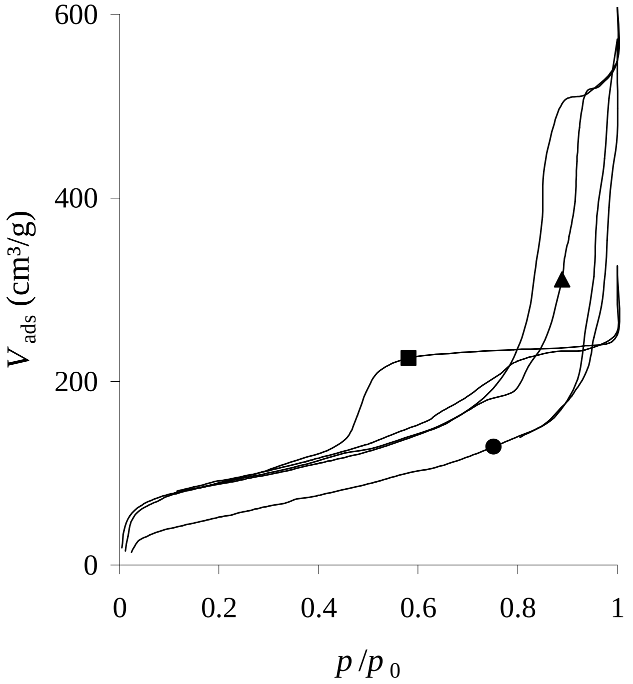

Fig. 9. Nitrogen adsorption-desorption isotherms. (●) *R/C* = 1000; (▲) *R/C* = 500; (■) *R/C* = 300.

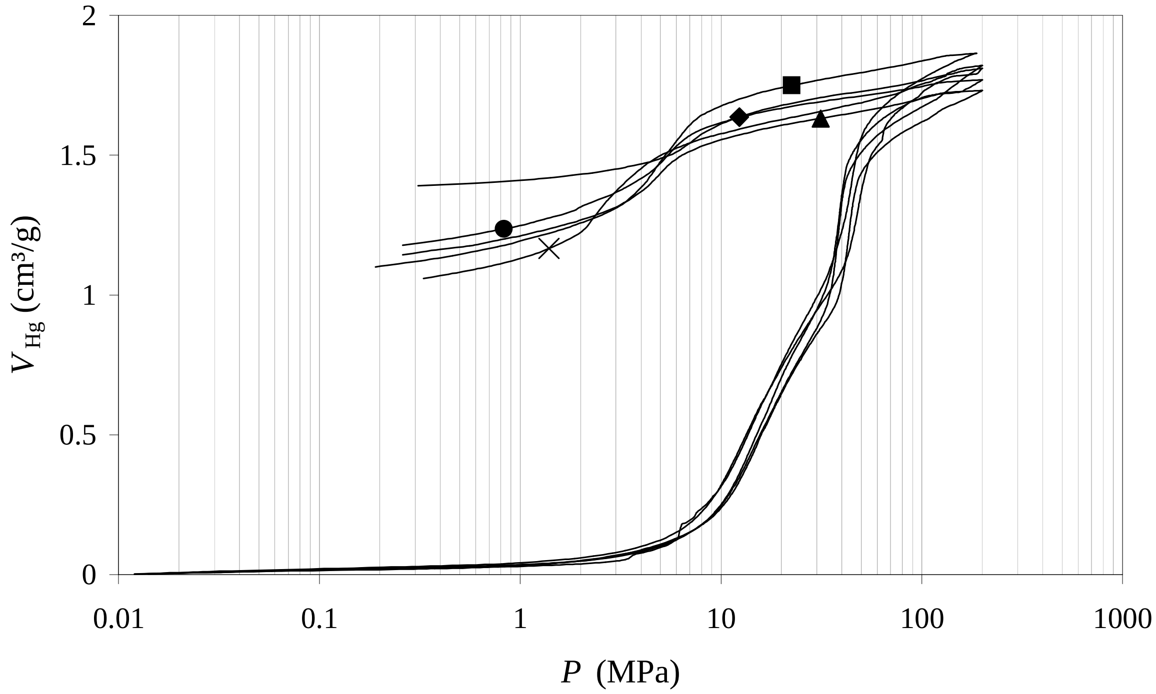

Fig. 10. Mercury porosimetry curves for samples synthesized with *R/C* = 1000. (■) X-1000-70-2; (◆) X-1000-115-1; (▲) X-1000-115-2; (●) X-1000-115-3; (×) X-1000-160-2.

4. Discussion

In the case of an ideal shrinkage, *i.e.* a volume reduction corresponding exactly to the volume of removed water, one can apply Eq. 3, where φ_0 is the initial solid concentration (Eq. 4), ρ_s and ρ_w are the skeletal density of the resin and the density of water, respectively. W_0 represents the initial water content, expressed on a dry basis.

$$\frac{V}{V_0} = \varphi_0 \left[1 + \frac{\rho_s}{\rho_w} \right] W \tag{3}$$

$$\varphi_0 = \frac{1}{1 + W_0 \frac{\rho_s}{\rho_w}} \tag{4}$$

Since all the samples were prepared with the same dilution ratio, *i.e.* the same initial solid concentration, φ_0, the linear part which is observed on Figure 1 for samples synthesised at *R/C* = 300 and *R/C* = 500 indicates a zone of ideal shrinkage, whose extent differs according to the *R/C* ratio. During this period, no porosity is created. From the value of the slope, φ_0 and ρ_s are estimated to 0.25 cm^3/cm^3 and 1.5 g/cm^3 which is in agreement with picnometry measurements. The final volume reduction is governed by the balance between the capillary tensions exerted by water in the pores and the mechanical resistance of the gel matrix [23]. The smaller the pore size in the initial wet matrix, the higher the capillary pressure, which explains the higher shrinkage extent observed at low *R/C* ratio. Indeed, according to the addition-condensation scheme governing the system, the mean pore size inside the wet network decreases when the pH of the precursors solution increases, *i.e.* when the *R/C* ratio decreases [2,24,25].

Each Krischer's curve is characterized by a plateau (constant drying flux) followed by a decreasing phase (Fig. 4). The plateau indicates that heat and mass transfer rates are controlled by extragranular limitations only, which are located in a boundary layer at the gas-solid interface. The internal transfer, *i.e.* water diffusion, mainly, is fast enough to ensure the feeding of the sample surface with water. A decrease of the drying flux means that internal transfer limitations appear. During a first decreasing zone, moisture gradients develop inside the solid. Internal and external transfer limitations occur simultaneously. Then, the evaporation front progressively recedes inside the solid: internal limitations totally control the drying process.

When external kinetics limitations are predominant, the mass flux can be expressed as the product of a mass transfer coefficient (k, m/s) and a driving potential as represented by Eq. 5 [26]. The driving potential corresponds to the difference between air humidities prevailing in the bulk of the drying agent (Y_a, $\mathrm{kg_{water}/kg_{air}}$) and at the air-solid interface ($Y_\mathrm{sat}(T_\mathrm{w})$, $\mathrm{kg_{water}/kg_{air}}$), *i.e.* the humidity of air saturated with water at the wet-bulb temperature, T_w, in purely convective conditions. ρ_a is the density of humid air ($\mathrm{kg/m^3}$).

$$F_\mathrm{c} = k\rho_\mathrm{a}\left[Y_\mathrm{sat}\left(T_\mathrm{w}\right) - Y_\mathrm{a}\right] \quad (5)$$

When the drying temperature increases, the wet-bulb temperature, T_w, increases, which leads to the augmentation of the humidity at the interface, $Y_\mathrm{sat}(T_\mathrm{w})$. As a consequence, the mass flux, F_c, also increases. It must be noted that the drying temperature affects the drying kinetics not only during the constant flux phase, but throughout the drying process. This can be attributed to the Arrhenius type behaviour of the water diffusion coefficient, which controls mass transfer during the last stages of drying. The influence of air velocity is related to the mass transfer coefficient, which evolves as a power law function of the air velocity [27]. When the curves overlap (Fig. 4), transfers are purely limited by internal resistances.

Two kinds of behaviour are observed in this work. For samples obtained with R/C = 300 and R/C = 500, the transition between the plateau and the decreasing flux period occurs at a water content which exactly corresponds to the end of shrinkage. During the contraction of the sample, the external surface remains saturated with water and the drying flux remains constant. For these samples, cracks appear after the end of shrinkage. In fact, internal diffusional limitations induce moisture gradients, which cause mechanical stresses [28]. Cracks progressively develop when stresses exceed the maximum breakage resistance of the material. Since the internal water diffusion coefficient decreases with decreasing pore sizes, the moisture gradients and, consequently, the resulting mechanical stresses, are steeper when the sample contains small pores. This explains why the breakage of the sample is favoured by low *R/C* values. For samples obtained with *R/C* = 1000, no clear transition can be observed because shrinkage is not important. It rather seems that, in this case, both internal and external transfer limitations coexist from the beginning to the end of drying. The evaporation front quickly recedes inside the solid. This result explains why the level of the flux plateau is lower for samples prepared with *R/C* = 1000 (Fig. 5). In the case of purely external transfer limitations, the same value of the constant flux, F_c, should have been observed for all the samples, whatever the *R/C* ratio. On the contrary, the zone where the curves are superimposed corresponds to pure internal limitations. The total drying time decreases with increasing *R/C* ratio, even though the mean drying flux is lower. This comes from the fact that the external area evolution *vs.* water content, which can be related to the shrinkage behaviour, depends on *R/C*. At *R/C* = 1000, the external area hardly decreases during the course of drying, remaining about two times larger than that of samples obtained with *R/C* = 300. This explains why shorter drying times are observed when *R/C* = 1000: the drying rate, *i.e.* the drying flux multiplied by the external exchange area, is higher. This is particularly critical for the removal of the last 10% of water: the drying fluxes are equal for the three synthesis conditions (Fig. 5) but the external exchange area increases with *R/C*.

The textural analysis shows that the pore texture of the dried gels does not depend on the drying conditions: the textural characteristics of the samples are completely pre-determined by the synthesis variables (*R/C*, mainly). The same is observed for the shrinkage behaviour. This means that the final texture can be entirely controlled by adequate synthesis conditions but also that the drying step can be accelerated to minimize the production time without altering the pore texture. However drying conditions have to be softened when the monolithicity of the sample is crucial. For samples containing small pores, *i.e.* when the gels are synthesized at low *R/C*, the drying operation can take more than 20 h.

5. Conclusions

Convective drying is a suitable method for the production of hyperporous organic materials from RF hydrogels. After pyrolysis, these materials develop high specific surface areas and pore volumes, as obtained when vacuum drying is used. Compared to vacuum drying, the convective process presents several advantages: costs are lower, the process is widely used in industry, and can be easily operated continuously at large scale.

The shrinkage underwent by the RF gels is isotropic and totally independent of the temperature and velocity of air used as drying agent. The shrinkage and the textural properties are completely determined by the original texture of the wet gel, which is itself fixed by the synthesis variables. Shrinkage is favoured by large capillary forces, *i.e.* small pore sizes. According to the addition-condensation scheme governing the system, the mean pore size inside the wet network decreases when the pH of the precursors solution increases, *i.e.* when the *R/C* ratio decreases [2]. This explains the observations: the lower the *R/C* value, the smaller the pore size and the higher the shrinkage.

The analysis of the Krischer’s curves shows two main drying phases. During the constant drying flux phase, corresponding to the shrinkage period, the transfers are controlled by external limitations: increasing the temperature or the air velocity leads to increasing the drying flux. The plateau is followed by a long decreasing flux period due to growing internal transfer limitations. At the beginning of this period, both external and internal transfer limitations coexist. The zone corresponding to pure internal transfer limitations is detected at the end of drying by the superimposition of the curves obtained at the same air temperature but at different air velocities.

The total weight loss is quite identical for all the samples prepared at the same dilution ratio (65-68% when *D* = 5.7). The drying time can be reduced by increasing the temperature and the velocity of air. When monolithicity is required, the drying flux must be carefully controlled: cracks appear when the drying conditions are too severe, especially at low *R/C* ratio. The drying temperature and air velocity being fixed at 160°C and 2 m/s respectively, about 1 h is needed to dry a 2.8 cm in diameter and 1 cm in height macroporous cylinder (pore width > 50 nm after drying). On the contrary, the same cylinder containing small mesopores (pore width ranging from 10 to 15 nm after drying) requires 20 h at 30°C and 2 m/s to reach complete dryness without the development of cracks.

The study of convective drying of RF gels enables us to consider the development of a basic and quite affordable industrial process for the production of porous carbon materials with tailored texture. This process avoids the most expensive steps of the drying techniques commonly used in studies found in the literature, like solvent exchanges or drying under supercritical conditions, and could be operated continuously under atmospheric pressure, at moderate temperature. The drying step could be directly followed or even coupled to pyrolysis in order to optimize the whole process. Our future work will be dedicated to the study of the influence of air humidity on both the drying kinetics and the cracking of the samples. Indeed, it is well-known in the agro-food industry that the use of air with high humidity for drying is a way to avoid cracking, but it also slows down the drying process. Finally, the production of larger, non symmetrical parts, which are more sensitive to mechanical stresses, will be investigated. This will require the development of a coupled hygro-thermo-mechanical model in order to determine and minimize the stress field and its evolution during drying.

Acknowlegments

A. Léonard is indebted to the Belgian Fonds National de la Recherche Scientifique (FNRS) for a position of Postdoctoral Researcher. The authors also thank the Belgian Fonds National de la Recherche Scientifique, the Région Wallonne - Direction Générale des Technologies, de la Recherche et de l'Energie -, the Ministère de la Communauté française - Direction de la Recherche Scientifique - and the Fonds de Bay for their financial support.

References

[1] Pekala RW. Low density resorcinol-formaldehyde aerogels. US Patent 4997804, 1991.

[2] Al Muhtaseb SA, Ritter JA. Preparation and properties of resorcinol-formaldehyde organic and carbon gels. Adv Mater 2003; 15(2):101-14.

[3] Kocklenberg R, Mathieu B, Blacher S, Pirard R, Pirard JP, Sobry R, et al. Texture control of freeze-dried resorcinol-formaldehyde gels. J Non-Cryst Solids 1998; 225(1):8-13.

[4] Mayer ST, Pekala RW. Method of low pressure and/or evaporative drying of aerogel. US Patent 5420168, WO 9422943, 1993.

[5] Pirard JP, Pirard R, Job N. Porous carbon material. Patent WO 03/026048 A1, 2003.

[6] Job N, Pirard R, Marien J, Pirard JP. Porous carbon xerogels with texture tailored by pH control during sol-gel process. Carbon 2004; 42(3):619-28.

[7] Job N, Panariello F, Marien J, Crine M, Pirard JP, Léonard A. Synthesis optimization of organic xerogels produced from convective air-drying of resorcinol-formaldehyde gels. J Non-Cryst Solids 2006; 352(1):24-34.

[8] Léonard A, Job N, Blacher S, Pirard JP, Crine M, Jomaa W. Suitability of convective air drying for the production of porous resorcinol-formaldehyde and carbon xerogels. Carbon 2005; 43(8):1808-11.

[9] Léonard A. Etude du séchage convectif de boues de station d'épuration - Suivi de la texture par microtomographie à rayons X. University of Liège, Belgium, PhD Thesis, 2003.

[10] Léonard A, Blacher S, Marchot P, Crine M. Use of X-ray microtomography to follow the convective heat drying of wastewater sludges. Dry Technol 2002; 20(4&5):1053-69.

[11] Kemp IC, Fyrh BC, Laurent S, Roques MA, Groenewold CE, Tsotsas E, et al. Methods for processing experimental drying kinetics data. Dry Technol 2001; 19(1):15-34.

[12] Léonard A, Blacher S, Marchot P, Pirard JP, Crine M. Measurement of shrinkage and cracks associated to convective drying of soft materials by X-ray microtomography. Dry Technol 2004; 22(7):1695-708.

[13] Vinegar HJ, Wellington SL. Tomographic imaging of three-phase flow experiments. Rev Sci Instrum 1987; 58(1):96-107.

[14] Sasov A, Van Dyck D. Desktop X-ray microscopy and microtomography. J Microsc 1998; 191:151-8.

[15] Léonard A, Blacher S, Marchot P, Pirard JP, Crine M. Image analysis of X-ray microtomograms of soft materials during convective drying. J Microsc 2003; 212(2):197-204.

[16] Lecloux AJ. Texture of catalysts. In: Anderson JR and Boudart M (editors). Catalysis: Science and Technology Vol. 2, Berlin; Springer, 1981; 171-230.

[17] Alié C, Pirard R, Lecloux AJ, Pirard JP. Preparation of low-density xerogels through additives to TEOS-based alcogels. J Non-Cryst Solids 1999; 246(3):216-28.

[18] Washburn EW. Note on a method of determining the distribution of pore sizes in a porous material. Proc Nat Acad Sci 1921; 115-6.

[19] Pirard R, Blacher S, Brouers F, Pirard JP. Interpretation of mercury porosimetry applied to aerogels. J Mater Res 1995; 10(8):2114-9.

[20] Pirard R, Heinrichs B, Pirard JP. Mercury porosimetry applied to low density xerogels. In: Mc Enaney B, Mays TJ, Rouquerol J, Rodriguez-Reinoso F, Sing KSW, and Unger KK (editors). Characterisation of Porous Solids IV, Cambridge, United Kingdom; The Royal Society of Chemistry, 1997; 460-6.

[21] Job N, Alié C, Pirard R., Pirard J. P. Non intrusive mercury porosimetry: pyrolysis of resorcinol-formaldehyde xerogel. Part Part Syst Charact (In Press).

[22] Pirard R, Alié C, Pirard JP. Specific behavior of sol-gel materials in mercury porosimetry: collapse and intrusion. In: Sakka S and Almeida RM (editors). Handbook of Sol-Gel Science and Technology, Vol II: Characterization of Sol-Gel Materials and Products, London; Kluwer Academic Publishers, 2004; 211-33.

[23] Smith DM, Scherer GW, Anderson JM. Shrinkage during drying of silica gel. J Non-Cryst Solids 1995; 188(3):191-206.

[24] Pekala RW, Kong FM. A synthetic route to organic aerogels: mechanism, structures and properties. Rev Phys Appl 1989; 24(C4):33-40.

[25] Pekala RW, Farmer JC, Alviso CT, Tran TD, Mayer ST, Miller JM, et al. Carbon aerogels for electrochemical applications. J Non-Cryst Solids 1998; 225(1):74-80.

[26] Mujumdar AS. Handbook of industrial drying. New York: Marcel Dekker. 1995.

[27] Geankoplis CJ. Transport processes and unit operations. Englewood Cliffs NJ: Prentice-Hall. 1993.

[28] Izumi M, Hayakawa KI. Heat and moisture transfer and hygrostress crack formation and propagation in cylindrical, elastoplastic food. Int J Heat Mass Transfer 1995; 38(6):1033-41.

Figure captions

Fig. 1. Shrinkage curves: influence of the drying temperature and *R/C* ratio. $v_{\mathrm{air}} = 2$ m/s. (●) X-1000-70-2; (●) X-1000-115-2; (▲) X-500-70-2; (△) X-500-92.5-2; (▲) X-500-115-2 (incomplete – breakage); (□) X-300-30-2; (■) X-300-70-2 (incomplete – breakage); (■) X-300-115-2 (incomplete – breakage).

Fig. 2. Shrinkage curves: influence of air velocity. *R/C* = 500 – *T* = 92.5°C. (□) X-500-92.5-1; (△) X-500-92.5-2; (○) X-500-92.5-3.

Fig. 3. Krischer’s curves: influence of the drying temperature at *R/C* = 500. (■) X-500-70-2; (▲) X-500-92.5-2; (●) X-500-115-2 (incomplete – breakage).

Fig. 4. Krischer’s curves: influence of the air velocity for *R/C* = 500. (▲) X-500-92.5-2; (×) X-500-92.5-1; (◆) X-500-92.5-3.

Fig. 5. Krischer's curves: influence of the *R/C* ratio on the drying flux. T = 70°C, v_{air} = 2 m/s. (●) X-1000-70-2; (▲) X-500-70-2; (■) X-300-70-2.

Fig. 6. Sample X-1000-115-2. Cross-sections at various stages of drying. (a) $W/W_0 = 0.23$, (b) $W/W_0 = 0.10$, (c) $W/W_0 = 0.001$.

Fig. 7. Sample X-300-30-2. Cross-sections before and after drying (a) $W/W_0 = 1$, (b) $W/W_0 = 0$ and (c) radiograph of the monolith at the end of drying at $W/W_0 = 0$.

Fig. 8. Sample X-300-70-2. Cross-sections before and after drying (a) $W/W_0 = 1$, (b) $W/W_0 = 0$ and (c) radiograph of the sample at the end of drying at $W/W_0 = 0$.

Fig. 9. Nitrogen adsorption-desorption isotherms. (●) $R/C = 1000$; (▲) $R/C = 500$; (■) $R/C = 300$.

Fig. 10. Mercury porosimetry curves for samples synthesized with $R/C = 1000$. (■) X-1000-70-2; (◆) X-1000-115-1; (▲) X-1000-115-2; (●) X-1000-115-3; (×) X-1000-160-2.

Table captions

Table 1.

Drying characteristics

Table 2.

Textural properties